ELSEVIER

Chemical Engineering Journal 74 (1999) 85–97

Chemical Engineering Journal

Nonequilibrium molecular dynamics simulation of a model carbon membrane separation of CH_4/H_2 mixtures

J.M.D. MacElroy*, M.J. Boyle

Department of Chemical Engineering, University College Dublin, Belfield, Dublin 4, Ireland

Abstract

A nonequilibrium molecular dynamics (NEMD) simulation technique is employed to investigate the transport of binary mixtures of hydrogen and methane through a model carbon membrane of varying thickness. Both forced flow simulations under a pressure gradient and isobaric counterdiffusion simulations are conducted in this work. The principal conclusions of these studies are: (i) pore entrance/exit effects may need to be taken into consideration in membrane design for hydrogen/hydrocarbon separations if the length of the controlling pores within the carbon membrane is of the order of one tenth of a micron or less; (ii) viscous (convective) flow contributions to the fluxes of the individual components of the mixture should be negligible for the carbon membranes currently in use; (iii) the cross-coefficients of diffusion appear to play a relatively minor role in the normal (pressure driven) hydrogen/methane membrane separation process however under isobaric conditions the simulation results suggest that hydrogen/methane cross-coupling plays a significant role in hindering the hydrogen counterdiffusion flux within carbon membranes containing long, narrow pores.

Keywords: Nonequilibrium molecular dynamics; Carbon membranes; Permeation

1. Introduction

The mathematical modelling of transport within porous media is one of the classical problems in chemical engineering with important implications for the design of adsorption columns, chromatographic separations, membrane separation units, and heterogeneous catalysis. The description of the fluxes of material within the media involved in these systems has been formulated in a variety of ways with the most widely accepted approach being the generalised theory developed by Mason and co-workers [1,2] (an extensive review of the Stefan–Maxwell theory of transport has also been provided recently by Krishna and Wesselingh [3]). Most frequently, with the exception of ideal gases, the species flux expressions contain coefficients which cannot easily be quantified and one method of approach to overcome this difficulty is direct molecular simulation.

While computer simulation has been employed to investigate transport in idealised micro-pore structures since the early 1980s it is only in the last few years that the simulation of diffusion and permeation within realistic media has been undertaken (for example, zeolites [4,5], silica [6–8], carbon molecular sieves [9–11], and polymeric materials [12,13]). The principal method employed in many of these studies was the equilibrium molecular dynamics (EMD) technique (see [14] for details) which can provide accurate estimates (to within a few per cent) for single particle transport properties (self or tracer diffusivities), and with somewhat less accuracy (standard errors of the order of 10–50%), for collective transport coefficients in homogeneous ('infinite') media. The significant errors associated with the determination of collective transport properties (e.g. mutual diffusivities, cross-coefficients and viscosities), and in particular, the limitation of the standard EMD procedure to homogeneous systems of infinite extent motivated the development of an alternative route to the determination of transport and permeation characteristics via nonequilibrium molecular dynamics (NEMD). This technique, developed independently in [15,16] and more recently in [17,18], involves the creation of stationary chemical potential gradients between two control volumes. The transport of material from one control volume to the other is then monitored during the simulation and the transport coefficients are obtained from direct measurements of the particle fluxes. It is this technique, and its application to a novel membrane separation process, which is of interest in this paper.

In Section 2, the basis for the NEMD simulation of the membrane separation of hydrogen and methane mixtures is described in detail. In this section we will also introduce a

*Corresponding author. Tel.: +353-1-706-1827; fax: +353-1-706-1177; e-mail: macelroy@ollamh.ucd.ie

1385-8947/99/$ – see front matter
PII: S1385-8947(99)00056-X

new algorithm which permits unambiguous simulation of transport under nonequilibrium 'isothermal' conditions within a physically stationary medium. In Section 3 the results for both finite membrane thickness (obtained via the NEMD technique) and EMD simulation within a membrane of infinite thickness are presented and discussed and in Section 4 our conclusions are summarised.

2. Simulation method

The carbon membrane modelled in this work is illustrated in Fig. 1. The fundamental cell for the molecular simulation consists of 10 basal graphite layers above and below a single isolated pore and this cell is periodically imaged in both the x and y directions. The membrane itself is therefore effectively a set of isolated pores each separated by 20 basal graphite layers in the x direction and of infinite breadth in the y direction. These dimensions are chosen to ensure that the flux of material through a given pore occurs independently of other pores in the system [19] and hence will provide specific details for individual intrapore and pore mouth effects in the transport process. Although this is a highly idealised system it does contain the principal elements needed (i) to illustrate the method of application of the NEMD technique and (ii) to ascertain those features of the hydrocarbon/hydrogen/carbon membrane permeation mechanism which play a central role in the industrial separation process. A single pore width of w=2.25Δ is chosen here for all of the simulations. This value of w is believed to be characteristic of the pores known to exist in the carbon membranes which have been developed for hydrocarbon/hydrogen separation processes [20,21].

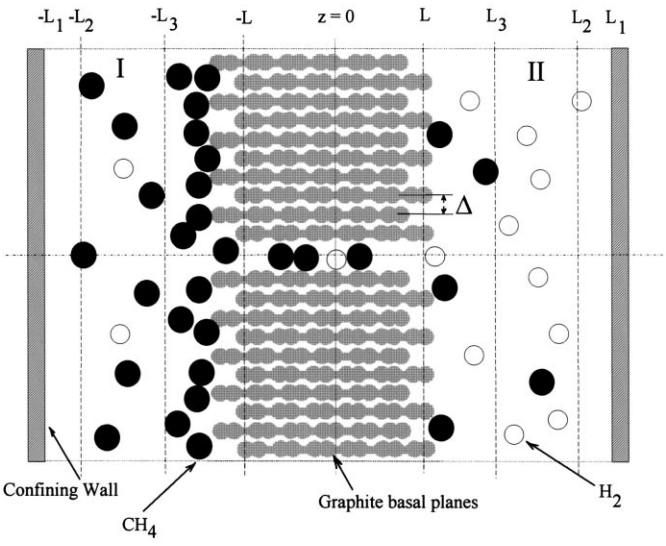

Fig. 1. The model finite length carbon slit pore. The magnitudes of L_1, L_2 and L_3 employed in the NMD simulations were (L+1.1 nm), (L+2.662 nm) and (L+3.342 nm), respectively, and the slit width between the two innermost basal planes was 2.25Δ, where Δ=0.335 nm.

In all of the computations the methane and hydrogen molecules are modelled as structureless particles which interact with each other and with the carbon atoms of the membrane via the truncated and shifted force form of the Lennard-Jones 12–6 potential:

$$\begin{aligned} \phi_{ij}^{SF}(r_{ij}) &= \phi_{ij}(r_{ij}) - \phi_{ij}(r_{cut}) - \left(\frac{d\phi_{ij}(r_{ij})}{dr_{ij}}\right)\Big|_{r_{cut}} (r_{ij} - r_{cut}), \qquad r_{ij} \le r_{cut} \\ &= 0, \qquad r_{ij} > r_{cut} \end{aligned} \tag{1a}$$

with

$$\phi_{ij}(r_{ij}) = 4\varepsilon_{ij}\left(\left(\frac{\sigma_{ij}}{r_{ij}}\right)^{12} - \left(\frac{\sigma_{ij}}{r_{ij}}\right)^{6}\right), \tag{1b}$$

where r_{cut} is the cut-off distance (2.5 σ_{ij} in the computations reported here) and σ_{ij} and ε_{ij} are the codiameter and potential well depth for particles i and j, respectively. The potential parameters employed in this work are summarised in Table 1 and the Lorentz–Berthelot rules, $\sigma_{ij} = (\sigma_{ii} + \sigma_{jj})/2$ and $\varepsilon_{ij} = \sqrt{(\varepsilon_{ii}\varepsilon_{jj})}$, have been employed to compute the terms for unlike species.

In general there are two stages to the simulation algorithm:

(i) *Initialisation*: The length of the pore is specified and the grand canonical ensemble Monte Carlo (GCMC) simulation method of Adams [24,25] (fixed μ, V and T) is applied independently to the two regions of the simulation box $-L_1 < z < 0$ and $0 < z < L_1$, respectively. The fluid components in both regions differ only with respect to their chemical potentials (or fugacities $\hat{f}_i$) and in all of the simulations the temperature was held constant at 273.15 K. At the end of this initialisation stage the cell volume in the region z<0 will contain a particular number of particles of both species and the cell volume in the region z>0 will contain a different number of particles of both species. In subsequent computations (see realisation below) the chemical potentials of both species are maintained at particular levels only within the control volumes I ($-L_2<z<-L_3$) and II ($L_3<z<L_2$).

(ii) *Realisation*: The particle velocities are now assigned from the Maxwell–Boltzmann distribution and the particle trajectories, at fixed particle number, are computed by solving the finite difference form of the equations of motion. The finite difference method employed in this work was the

Table 1
Lennard-Jones (12–6) interaction parameters for the carbon/hydrogen/methane system (both the hydrogen and methane particles are treated as united atom structures)

Particle i/particle j	ε_{ij}/k (K)	σ_{ij} (nm)
C/C[a]	28.0	0.340
H_2/H_2[b]	37.0	0.2928
CH_4/CH_4[b]	148.2	0.3817

[a] From Ref. [22].
[b] From Ref. [23].

Verlet algorithm [26] and will be described below in more detail during the discussion of the dynamical interaction between the carbon atoms and the fluid particles. As the particle trajectories evolve the particle depletion or accumulation within control volumes I and II is counterbalanced by periodically freezing the state of the system and conducting a short sequence of GCMC destruction/creation events on the fluid mixtures within control volumes I and II. For a given component i the prescription for the particle destruction/creation sequence is

(a) *Destruction*: acceptance if

$$\frac{\mathscr{P}_\beta}{\mathscr{P}_\alpha} = \frac{N_i RT}{\hat{f}_i V}\exp\left(-\frac{\Delta\Phi_{\alpha\beta}}{kT}\right) > \xi. \tag{2a}$$

(b) *Creation*: acceptance if

$$\frac{\mathscr{P}_\beta}{\mathscr{P}_\alpha} = \frac{\hat{f}_i V}{(N_i+1)RT}\exp\left(-\frac{\Delta\Phi_{\alpha\beta}}{kT}\right) > \xi, \tag{2b}$$

where $\mathscr{P}_\beta/\mathscr{P}_\alpha$ is the relative probability of observing two states β and α differing in potential energy by $\Delta\Phi_{\alpha\beta}$ and particle number by 1, N_i is the number of particles of component i present in state α, and ξ is a random number uniformly distributed on $\{0,1\}$. For the conditions employed during the simulations conducted in this work it was found that a sequence of 50 destruction or creation events (the type of event being selected randomly) every 10 time steps during the finite difference solution of the equations of motion provided excellent control of the thermodynamic states of the species in volumes I and II. After each sequence of destruction/creation events all of the newly created particles within control volumes I and II are assigned velocities from the appropriate Maxwell–Boltzmann distribution function at the specified temperature (the velocities and coordinates of all other particles are still stored and remain untouched) and the forces on each particle are evaluated from their known coordinates.

As noted above the Verlet finite difference algorithm [26] was employed to solve the equations of motion of the particles. This algorithm requires the initial centre of mass positions, velocities and accelerations (based on force calculations using Eqs. (1a) and (1b)), of each particle i:

$$\boldsymbol{r}_i(\delta t) = \boldsymbol{r}_i(0) + \boldsymbol{v}_i(0)\delta t + \frac{1}{2}\boldsymbol{a}_i(0)\delta t^2, \tag{3a}$$

Thereafter the particle positions are computed using

$$\boldsymbol{r}_i(t+\delta t) = 2\boldsymbol{r}_i(t) - \boldsymbol{r}_i(t-\delta t) + \boldsymbol{a}_i(t)\delta t^2, \tag{3b}$$

with the velocity at time t given by

$$\boldsymbol{v}_i(t) = \frac{\boldsymbol{r}_i(t+\delta t) - \boldsymbol{r}_i(t-\delta t)}{2\delta t}. \tag{3c}$$

Two modifications of this algorithm are required to restart the computations at intermittent points during the implementation of the code: (i) after performing a sequence of destruction/creation events on the particles in control volumes I and II and (ii) after a thermal collision (to be described below) between a methane or hydrogen particle and a carbon atom of the solid (in this work the carbon atoms are held fixed in space).

In case (i) the position coordinates at time $t - \delta t$ for each of the newly created particles (created at time t) within control volumes I and II are obtained using

$$\boldsymbol{r}_i(t-\delta t) = \boldsymbol{r}_i(t) - \boldsymbol{v}_i(t)\delta t + \frac{1}{2}\boldsymbol{a}_i(t)\delta t^2, \tag{4}$$

where $\boldsymbol{v}_i(t)$ is the velocity of the particle preselected from the Maxwell–Boltzmann distribution function.

For case (ii) the following conditions need to be considered. During the evolution of the particle trajectories a novel fluid/solid thermal diffuse scattering algorithm is employed during the simulations to ensure that transport within the pore structure occurs under fluid/solid thermally equilibrated conditions irrespective of how many particles are within the pore at any given time. The method involves changing the momentum and kinetic energy of the methane or hydrogen particles at the fluid particle/carbon atom potential minimum in such a way that the particles are reflected from the collision plane according to the cosine law of diffuse scattering while simultaneously satisfying conditions corresponding to thermal equilibration with the carbon surface. This thermal diffuse scattering algorithm is best considered with reference to Fig. 2.

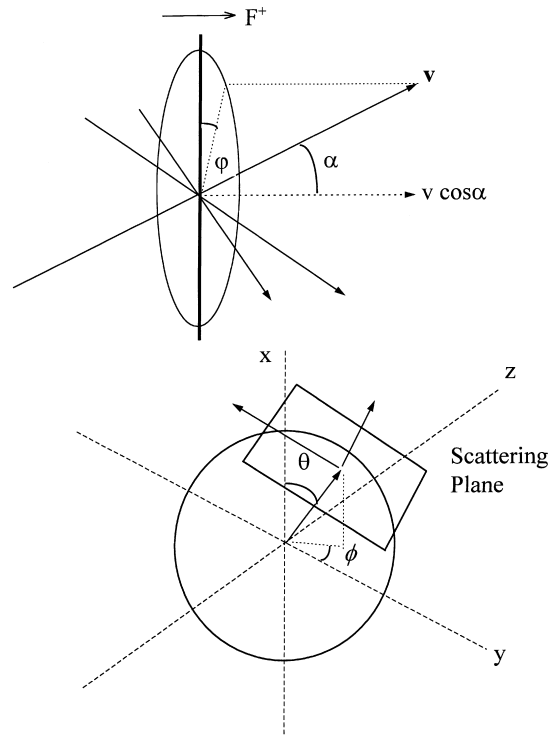

Fig. 2. Fluid particle/carbon atom thermal scattering algorithm. The top diagram illustrates the coordinate frame for the Maxwellian particle flux taking place from left to right and the lower diagram shows this scattering plane tangential to the sphere whose radius corresponds to $2^{1/6}\sigma_{ic}$.

In a fluid at local thermodynamic equilibrium the magnitude of the differential flux of particles travelling from left to right through a plane centred at $\boldsymbol{r}$ is

$$dF^{+}=n(\boldsymbol{r})\left(\frac{m}{2\pi kT}\right)^{3/2}\exp\left(-\frac{mv^2}{2kT}\right)(v\cos\alpha)v^2\,dv\sin\alpha\,d\alpha\,d\varphi, \tag{5a}$$

where $n(\boldsymbol{r})$ is the local number density of the particles, m is their mass, v is the magnitude of the particle velocity and α and φ are the polar angles describing the particle velocity vector. For computational purposes this expression is more conveniently rewritten in the following form:

$$dF^{+}=\left(\frac{1}{4}n(\boldsymbol{r})\bar{v}\right)d\left[(v^{*^2}+1)\exp(-v^{*^2})\right]d\left[\cos^2\alpha\right]d[\varphi/2\pi], \tag{5b}$$

$$=\left(\frac{1}{4}n(\boldsymbol{r})\bar{v}\right)G(\xi_1,\xi_2,\xi_3)\,d\xi_1\,d\xi_2\,d\xi_3, \tag{5c}$$

where G is the three-dimensional uniform distribution function and ξ_1, ξ_2 and ξ_3 are random numbers distributed on $\{0,1\}$. This result demonstrates that in order to simulate equilibrated thermal scattering from a surface one need only sample three uniformly distributed random numbers and compute the velocity components according to

$$v_1=v^*\cos(2\pi\xi_3)\sqrt{1-\xi_2}, \tag{6a}$$

$$v_2=v^*\sin(2\pi\xi_3)\sqrt{1-\xi_2}, \tag{6b}$$

$$v_3=v^*\sqrt{\xi_2}, \tag{6c}$$

where the dimensionless speed $v^*=v\sqrt{m/2kT}$ is obtained from

$$\xi_1=(v^{*^2}+1)\exp(-v^{*^2}). \tag{6d}$$

(The latter is not required for elastic scattering [27,28]). This method ensures that the particles emanating from a plane are scattered with a Maxwellian distribution of molecular speeds. It is also important to note that this thermal effect only takes place during a collision with the solid surface atoms and therefore in general does not interfere with the pore cross-section dependence of the local particle flux. Since the carbon atoms are explicitly held fixed in space this results in a significant savings in computer time. The inclusion of the high frequency vibrational motion of the carbon atoms would require very small time steps and hence very long simulation runs to properly model the system dynamics.

It is clear from the expression for the differential flux, Eq. (5c), that the scattering plane must be defined at a specific location $\boldsymbol{r}$ and in this work the plane was placed at the position of the fluid particle/carbon atom potential minimum, $\boldsymbol{r}_{ic}=2^{1/6}\sigma_{ic}$ (see Fig. 2). During the simulations a procedure was employed to determine, a posteriori, if, during a given time step, the relative separation of a fluid particle and carbon atom satisfied this condition. If so, the particle trajectory was retraced to determine the point of 'collision' by using Newton's method to solve the expression:

$$\left|\boldsymbol{r}_i(t)-\boldsymbol{r}_c+\boldsymbol{v}_i(t)f\delta t+\frac{1}{2}\boldsymbol{a}_i(t)(f\delta t)^2\right|^2=(2^{1/6}\sigma_{ic})^2, \tag{7}$$

where $0<f<1$. Once the minimum value of f had been determined for a given i-c pair, particle i was advanced through time $f_{\min}\delta t$ and its velocity components were changed according to the prescription described in Eqs. (6a), (6b), (6c) and (6d). The completion of the time step was then achieved by moving the particle to

$$\boldsymbol{r}_i(t+\delta t)=\boldsymbol{r}_i(t+f\delta t)+\boldsymbol{v}_i^{\text{scatt}}(1-f)\delta t, \tag{8}$$

where $\boldsymbol{v}_i^{\text{scatt}}$ is the post-collisional velocity of the scattered particle. This procedure was applied to each fluid particle independently during a given time step, and if necessary, repeated when multiple 'collisions' for the same particle were predicted to occur within the time step. One additional detail which was included in the analysis was that the direction of approach of a given particle i to the potential minimum was taken to be irrelevant. The post-collisional normal to the tangent plane illustrated in Fig. 2 was selected randomly and therefore the fluid particle could either be scattered away from the carbon atom or towards it. This ensures the configurational properties of adsorbed fluid are unaffected by the choice of scattering algorithm.

At the end of a time step in which a 'collision' or 'collisions' occurred between a fluid particle and a carbon atom the Verlet algorithm was restarted by computing the position at t using the approximation:

$$\boldsymbol{r}_i(t)=\boldsymbol{r}_i(t+\delta t)-\boldsymbol{v}_i^{\text{scatt}}\delta t. \tag{9}$$

In all of the NEMD simulations conducted in this work the time step δt was taken to be 5 fs. An initial period was allowed to ensure steady state had been reached and the length of time allocated for these computations was usually 2.5 ns for the shortest pores increasing to 10 ns for the longest pores investigated. Production runs of twice this length were employed to sample the particle fluxes.

Three isothermal case studies were undertaken to compute the methane and hydrogen permeabilities as functions of pore length, $2L$, within membranes of the type illustrated in Fig. 1.

With the fugacity defined in dimensionless form as

$$\hat{f}_i=f_i^0(\Delta^3/kT)\exp((\mu_i-\mu_i^0(T))/kT), \tag{10}$$

where f_i^0 is a reference fugacity of one pressure unit (0.1 MPa) for pure i, these simulations involved:

1. Forced flow: $\hat{f}_1(\text{I})=0.0343$, $\hat{f}_1(\text{II})=0.001707$, and $\hat{f}_2=\text{constant}=0.00765$.
2. Forced flow: $\hat{f}_2(\text{I})=0.0343$, $\hat{f}_2(\text{II})=0.001707$, and $\hat{f}_1=\text{constant}=0.00765$.
3. Isobaric counterdiffusion: $\hat{f}_1(\text{I})=0.0343$, $\hat{f}_1(\text{II})=0.001707$, and $\hat{f}_2(\text{I})=0.001707$ and $\hat{f}_2(\text{II})=0.0364$.

The dimensionless units for the fugacity (kT/Δ^3=100.3 MPa at 273.15 K) defined above are employed throughout this paper.

In each case the fluxes were determined by simply counting the net number of particles which cross a given plane within the system (three planes at $z=-L$, $z=0$, and $z=L$ were considered here to obtain average fluxes) and the effective permeabilities, P_i, were determined from the flux expression:

$$J_i = \frac{P_i}{(2L)}\Delta\hat{f}_i, \tag{11}$$

where $\Delta\hat{f}_i$ is the fugacity difference between control volumes I and II.

In addition to the nonequilibrium MD simulations, a number of equilibrium GCMC and molecular dynamics (EMD) simulations were conducted on a pore of infinite length in the z as well as y directions to investigate the equilibrium adsorption characteristics and the infinite system diffusivities for binary mixtures of methane and hydrogen. The GCMC method employed in these computations was the same as that proposed by Adams [24,25] and involved random particle displacements in addition to the destruction and creation events described above. The equilibrium MD simulations also employed the Verlet algorithm supplemented with the thermal diffuse scattering algorithm for particle/carbon atom interactions. In these computations the diffusion coefficients D_{ij} appearing in the flux expressions:

$$\begin{aligned}\boldsymbol{J}_1 &= -L_{11}\nabla\mu_1 - L_{12}\nabla\mu_2 - \frac{B_0 n_1}{\eta}\nabla p \\ &= -\frac{D_{11}n_1}{kT}\nabla\mu_1 - \frac{D_{12}n_2}{kT}\nabla\mu_2 - \frac{B_0 n_1}{\eta}\nabla p,\end{aligned} \tag{12a}$$

$$\begin{aligned}\boldsymbol{J}_2 &= -L_{21}\nabla\mu_1 - L_{22}\nabla\mu_2 - \frac{B_0 n_2}{\eta}\nabla p \\ &= -\frac{D_{21}n_1}{kT}\nabla\mu_1 - \frac{D_{22}n_2}{kT}\nabla\mu_2 - \frac{B_0 n_2}{\eta}\nabla p,\end{aligned} \tag{12b}$$

were determined using Einstein's equation:

$$D_{ij} = \frac{1}{4N_j kT}\lim_{t\to\infty}\frac{d}{dt}\left\langle \sum_{\alpha=1}^{N_i}(\boldsymbol{r}_\alpha(t)-\boldsymbol{r}_\alpha(0))\cdot\sum_{\beta=1}^{N_j}(\boldsymbol{r}_\beta(t)-\boldsymbol{r}_\beta(0))\right\rangle, \tag{13}$$

where the term inside the angular brackets is the time–displacement correlation function (TDF) of the positions of the particles which is averaged over the equilibrium ensemble.

In the equilibrium simulations the dimensions of the fundamental cells in the y and z directions varied from $\{L_y,\ L_z\}=\{3.69\text{ nm},\ 4.12\text{ nm}\}$ to $\{L_y,\ L_z\}=\{11.81\text{ nm},\ 12.50\text{ nm}\}$ depending on pore loading. These cell sizes ensured a minimum of approximately 100 particles of a given binary mixture within the fundamental cell during the GCMC or EMD productions runs.

3. Results

3.1. Equilibrium simulation results

Two sets of GCMC simulation runs were conducted to determine the equilibrium adsorption characteristics for mixtures of methane and hydrogen within the narrow carbon pore. In the first set of computations the fugacity of hydrogen was fixed at $\hat{f}_2$=0.00765 and the methane fugacities were varied over the range $0.000628 < \hat{f}_i < 0.0932$. The second set of simulations were conducted for $\hat{f}_1 = 0.00765$ and over the range $0.001707 < \hat{f}_2 < 0.0932$ and the results obtained from these computations are shown in Fig. 3. In addition, Monte Carlo integration [14] was employed to independently determine the Henry's law constants K_i for both components and the values so obtained were K_1=304.5 and K_2=5.94 at 273.15 K, in units of Δ^3/kT.

The full lines shown in Fig. 3 are the results obtained by successfully fitting the raw data to a model for mixture adsorption proposed by Ruthven et al. [29]. This model entails sitewise adsorption with multiple occupancy and for the conditions prevailing in the present work, geometric considerations of the adsorption space imply: (i) the number of sites per unit volume within the two-dimensional carbon slit is, in dimensionless units, $n_m^* = n_m\Delta^3 = 0.238$ and (ii) only one methane particle at most can occupy a site whereas a pair of hydrogen particles or a single hydrogen particle and a methane particle can simultaneously occupy a given site. The isotherms for both species under these

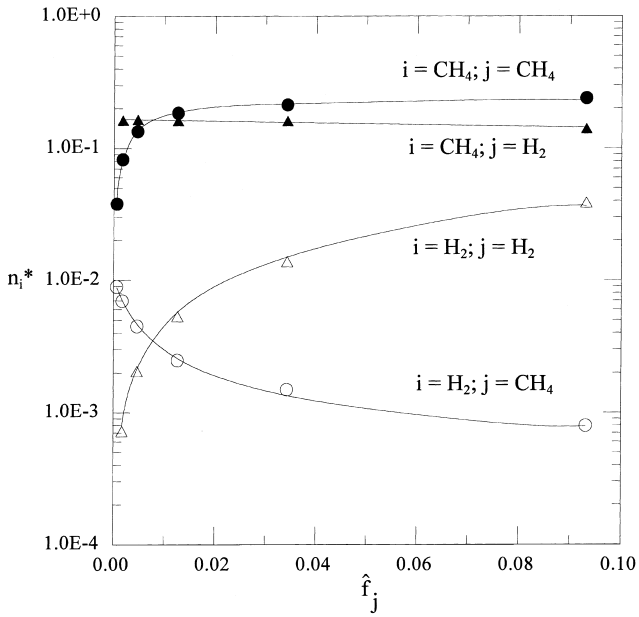

Fig. 3. GCMC adsorption isotherms for methane–hydrogen mixtures. n_i^* is based on volume 2.25Δ. Surface area and $\hat{f}_j$ is in units of Δ^3/kT. The full lines are the results correlated by Eqs. (14a) and (14b).

conditions are given by

$$\frac{n_1^*}{n_m^*} = \frac{K_1\hat{f}_1(1+\alpha_1\hat{f}_2)}{1+K_1\hat{f}_1(1+\alpha_1\hat{f}_2)+K_2\hat{f}_2(1+\alpha_2\hat{f}_2)} \quad \text{(methane)} \tag{14a}$$

$$\frac{n_2^*}{n_m^*} = \frac{K_2\hat{f}_2(1+2\alpha_2\hat{f}_2)+K_1\alpha_1\hat{f}_1\hat{f}_2}{1+K_1\hat{f}_1(1+\alpha_1\hat{f}_2)+K_2\hat{f}_2(1+\alpha_2\hat{f}_2)} \quad \text{(hydrogen)}. \tag{14b}$$

The coefficients α_i arise due to multiple occupancy associated with the hydrogen particles. These parameters were the only quantities employed in fitting Eqs. (14a) and (14b) to the data and the results obtained from a nonlinear fit of all of the data are $\alpha_1=0.239\Delta^3/kT$ and $\alpha_2=0$ (the latter result implies that while sterically feasible, two hydrogen particles are unlikely to occupy the same site although it may be preferable to simply consider Eqs. (14a) and (14b) as correlative rather than predictive in view of the approximations of the model).

In Fig. 4 we report examples of the number density profiles for hydrogen and methane obtained from the GCMC simulations. These results demonstrate that the adsorbed fluid mixture within the 2.25Δ pore is truly two-dimensional. The very shallow minimum in the hydrogen profile at the centre of the pore arises due to the smaller size of the H_2 particles and illustrates the weak adsorption effects experienced by this component. Also shown in this figure (open and filled triangles) are the corresponding profiles obtained from the EMD simulations and the excellent agreement between both sets of results confirms the ability of the thermal diffuse scattering algorithm to produce isothermal configurational properties. We should add that similar agreement between GCMC profiles and thermal diffuse scattering EMD profiles was obtained irrespective of the number of fluid particles involved in the simulation, a result which is not provided by microcanonical (fixed N, V and E) EMD simulation of small numbers of particles within a stationary medium.

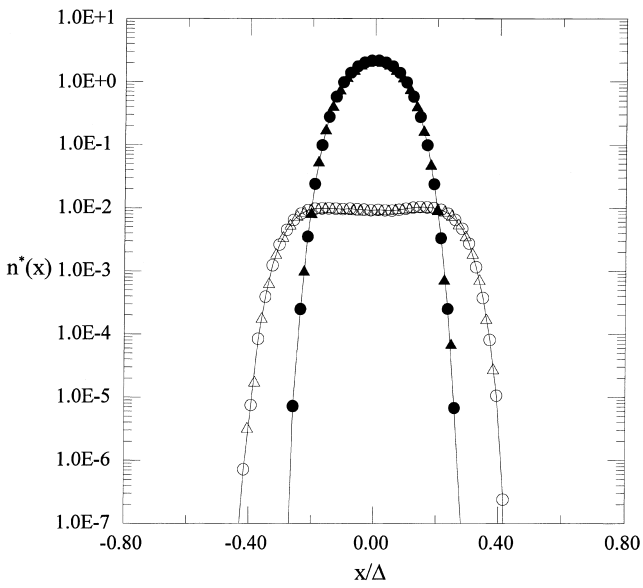

Fig. 4. Density profiles across the slit pore for CH_4 (filled symbols) and H_2 (open symbols) from GCMC (circles) and thermal diffuse scattering EMD (triangles).

The diffusion coefficients computed from the EMD particle trajectories using Eq. (13) for the complete range of thermodynamic conditions investigated via GCMC as specified in Fig. 3 are reported in Fig. 5(a,b). The last of these figures, Fig. 5(c), contains a limited number of additional diffusivities, including the cross-diffusion coefficient D_{12}, which were specifically computed for conditions in which the sum $\hat{f}_1+\hat{f}_2 = \text{constant} = 0.037$ and the reasons for this will become clear later in Section 3.2. (It should be noted that the cross-diffusion coefficient is very difficult to determine with any accuracy and the results provided in Fig. 5(c) were computed from trajectories which were at least 0.5 ns in length.) Furthermore, for comparative purposes in Fig. 5(a,b) we also report results for the tracer diffusion coefficients $D_{i^*i^*}$ which are primarily of interest in spectroscopic studies of particle mobility (for example, NMR). However, of most concern here are the phenomenological coefficients D_{ij} which are central to the evaluation of transport under industrial processing conditions.

On the basis of the general theory of transport within porous media proposed by Mason and co-workers [1,2] it may be shown that the phenomenological diffusion coefficients D_{ij} defined in Eqs. (12a) and (12b) are related to the three Stefan–Maxwell pair diffusivities $Đ_{12}$, $Đ_{1M}$ and $Đ_{2M}$ by the expressions (see also [3,7,27,28]):

$$D_{11} = \frac{(x_1/Đ_{12})+(1/Đ_{2M})}{((x_1/Đ_{1M})+(x_2/Đ_{2M}))(1/Đ_{12})+(1/Đ_{1M}Đ_{2M})}, \tag{16a}$$

$$D_{22} = \frac{(x_2/Đ_{12})+(1/Đ_{1M})}{((x_1/Đ_{1M})+(x_2/Đ_{2M}))(1/Đ_{12})+(1/Đ_{1M}Đ_{2M})}, \tag{16b}$$

$$D_{12} = \frac{(x_1/Đ_{12})}{((x_1/Đ_{1M})+(x_2/Đ_{2M}))(1/Đ_{12})+1/Đ_{1M}Đ_{2M}}, \tag{16c}$$

and

$$D_{21} = \frac{x_2}{x_1}D_{12}, \tag{16d}$$

where the diffusivity $Đ_{12}$ is the interdiffusion coefficient for the pair of diffusing species 1 and 2 and the coefficients $Đ_{iM}$ are the diffusion coefficients of the individual components relative to the stationary porous medium (in the limit $n_i \to 0$ these coefficients are the free particle diffusion coefficients). For an adsorbed supercritical gas mixture in which core repulsion interactions are dominant the two-dimensional kinetic theory of Lee and O'Connell [30]

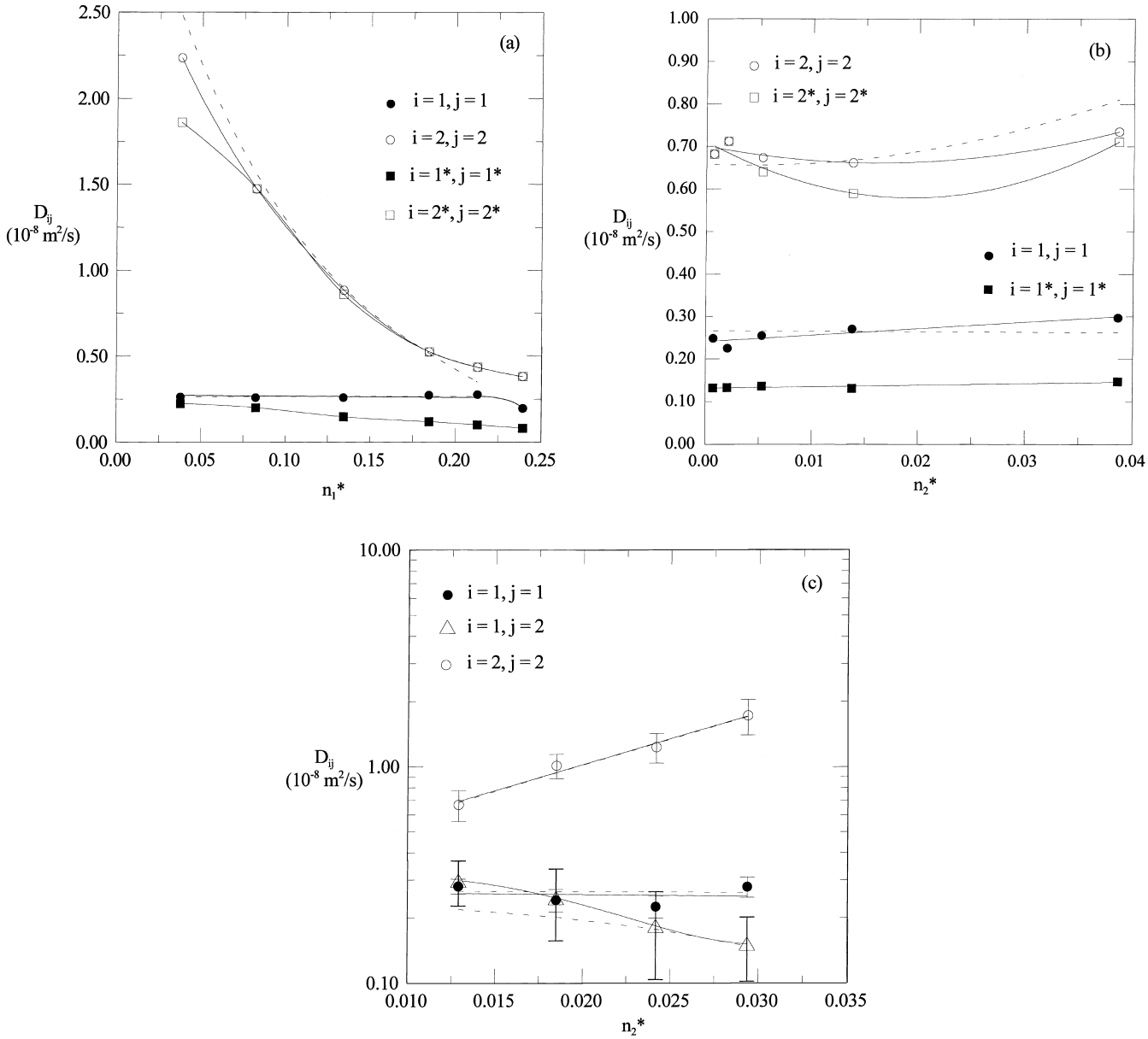

Fig. 5. Phenomenological diffusivities as functions of loading for (a) fixed hydrogen fugacity; (b) fixed methane fugacity; (c) isobaric conditions. The zero loading values for D_{11} and D_{22} ($n_1+n_2\rightarrow 0$) are $D_{11}=0.245\times10^{-8}$ m^2/s and $D_{22}=2.98\times10^{-8}$ m^2/s and the dashed lines represent the fit of the data for the methane diffusivity D_{11}, the hydrogen diffusivity D_{22} and the cross-diffusion coefficient D_{12} to the kinetic model of Lee and O'Connell [30].

may be adapted to multicomponent mixtures to obtain approximate expressions for the individual pair diffusivities:

$$Đ_{12} = \sqrt{\left(\frac{kT}{2\pi}\frac{(m_1+m_2)}{m_1 m_2}\right)}\frac{1}{n\sigma_{12}g(\sigma_{12})E_{12}}, \tag{17a}$$

and

$$Đ_{i\mathrm{M}} = \sqrt{\left(\frac{kT}{2\pi m_i}\right)}\frac{1}{n_s\sigma_s E_{is}}, \tag{17b}$$

where m_i is the mass of particle i, the quantity $g(\sigma_{12})$ is the contact pair correlation function for particles of species 1 and 2, and E_{12} and E_{is} are parameters which depend only on temperature, and to a first approximation, are independent of loading. Within the scope of this model, n in Eq. (17a) refers to the total *fluid* number density (per unit area) and n_s is the two-dimensional number density of the sites within the pore. A comparatively simple expression may be obtained from scaled particle theory [31] for the two-dimensional contact pair correlation function for the fluid pair 1–2 and in the following it will be assumed that the only fitting parameters involved at the given temperature are E_{12}, $Đ_{1\mathrm{M}}$ and $Đ_{2\mathrm{M}}$. The expression for $g(\sigma_{12})$ provided by scaled particle theory is

$$g(\sigma_{12}) = \frac{1-(\pi/4)\sum n_i\sigma_i^2 + (\pi/4)(\sigma_1\sigma_2/(\sigma_1+\sigma_2))\sum n_i\sigma_i}{(1-(\pi/4)\sum n_i\sigma_i^2)^2}, \quad (18)$$

where the summations extend over all fluid species.

The results obtained from a nonlinear regression of all of the simulation data with the exception of the highest methane loading results for D_{11} and D_{22} at $n_1^* = 0.29$ are shown as dashed lines in Fig. 5((a)–(c)). The best fit parameter estimates were E_{12}=20.7, $Đ_{1M}$=0.266×10^{-8} m^2/s, and $Đ_{2M}$=3.85×10^{-8} m^2/s and as may be seen from the dashed lines in these figures the concentration dependence of the individual phenomenological diffusion coefficients (predicted primarily by the group of terms $n\sigma_{12}g(\sigma_{12})$ in the denominator of Eq. (17a)) is well correlated by the model (in fitting the data it was also found that reported *hard-sphere* diameters for methane (0.4187 nm) and hydrogen (0.2745 nm) [32] provided the best fit). The large estimate for E_{12} is not unexpected in view of the comparatively strong sorptive interactions between the methane and the carbon substrate. Moreover, the loading independence of $Đ_{1M}$ (which is essentially equal to D_{11}) suggested by the model of Lee and O'Connell [30] is supported by the results (an independent simulation of the zero loading state gave a value $Đ_{1M}$=0.245×10^{-8} m^2/s). A similar though less favour- able comparison can be made between the fitted hydrogen diffusivity $Đ_{2M}$ and the zero loading result $Đ_{2M}$= 2.98×10^{-8} m^2/s. The larger value of the fitted estimate suggests that a small degree of screening exists which effectively lowers the hydrogen/carbon interaction parameter E_{is}.

3.2. Nonequilibrium simulation results

The results obtained from the NEMD simulations for the permeabilities (see Eq. (11)) of both species in the three case studies considered in this work are shown as the open (hydrogen) and filled (methane) circles in Fig. 6. Also shown in this figure are the results predicted for pores of infinite length which were determined as follows. In the absence of pore entrance and exit effects the one-dimensional fluxes when one of the chemical potentials is held constant are given by

$$J_i = -D_{ii}\frac{n_i}{kT}\frac{d\mu_i}{dz} - \frac{B_0 n_i}{\eta}\frac{dp}{dz}, \quad (i=1,2) \quad (19a)$$

$$J_i = -D_{ij}\frac{n_j}{kT}\frac{d\mu_j}{dz} - \frac{B_0 n_i}{\eta}\frac{dp}{dz}, \quad (i,j=1,2;\ i\neq j) \quad (19b)$$

and for isobaric counterdiffusion:

$$J_i = -D_{ii}\frac{n_i}{kT}\frac{d\mu_i}{dz} - D_{ij}\frac{n_j}{kT}\frac{d\mu_j}{dz}, \quad (i,j=1,2) \quad (19c)$$

Before discussing the explicit permeability data shown in Fig. 6 it is of particular interest to first consider Eq. (19b) since it implies that a flux of i will be observed in the presence of a gradient in the chemical potential of the other component. The fact that no such coupled transport was observed in any of the forced flow NEMD simulations conducted in this work suggests that the contributions from the cross-coefficient terms, D_{ij}, and the viscous (convective) terms to the flux of both components are negligible for the conditions investigated in the (a) and (b) series of runs (note that in pressure units the magnitude of pressure differential employed in the force flow simulations is of the order of 3 MPa). Since D_{21} (see Eqs. (16c) and (16d)) and n_2 are both negligibly small for the conditions considered in this work then it is not surprising that a hydrogen flux arising from a coupling with a methane chemical potential gradient is not observed. For methane at fixed methane fugacity and variable hydrogen fugacity however this is not immediately clear. From the results reported in Section 3.1 we have to a

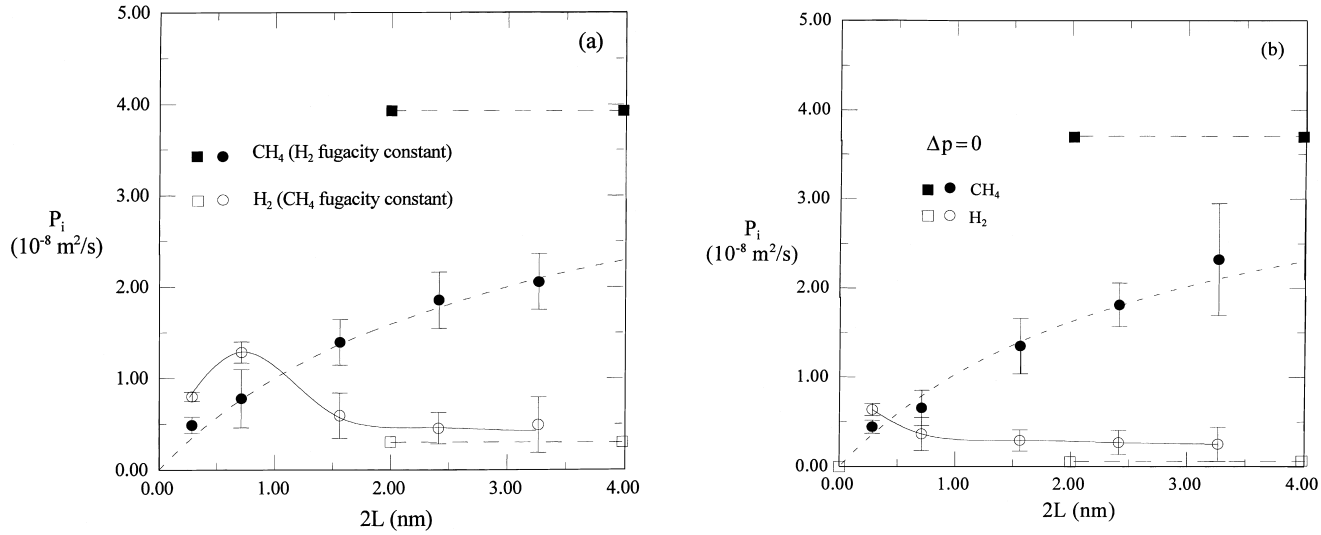

Fig. 6. NEMD methane and hydrogen permeabilities obtained from (a) pressure driven transport and (b) isobaric counterdiffusion. The dashed lines tagged by open and filled squares correspond to the predicted results for infinitely long pores and the dashed line through the filled circles corresponds to Eq. (27).

good approximation $D_{12}\sim Đ_{1M}\sim D_{11}$. Therefore if, for the moment, it is assumed that the viscous terms are negligible then, given that the same driving forces are used in both sets of forced flow simulations, one may write approximately

$$\frac{J_1(\hat{f}_1 = \text{constant})}{J_1(\hat{f}_2 = \text{constant})} \approx \frac{n_2/n_{2B}}{n_1/n_{1B}} = S_{21}. \tag{20}$$

Thus, in the absence of viscous effects, the methane flux arising from a gradient in the hydrogen chemical potential should be very small since the selectivity S_{21} is ~0.02. In contrast, the local number density of the methane within the pores may be expected to be quite large and therefore since no coupled methane transport was actually observed it may be concluded that convection does not play a significant role in the permeation process. This will be independently verified below.

These observations significantly simplify the analysis for pores of infinite length with the following results. For the range of conditions involved in the two cases of forced flow it is observed from both Fig. 5(a,b) that for fixed $\hat{f}_1$ and variable $\hat{f}_2$ ($0.0 < n_2^* < 0.014$) the hydrogen phenomenological diffusion coefficient, D_{22}, is only weakly dependent on loading and for fixed $\hat{f}_2$ and variable $\hat{f}_1$ ($0.0 < n_1^* < 0.215$) the methane coefficient, D_{11}, is independent of loading. Using the local equilibrium adsorption isotherms (Eqs. (14a) and (14b))), the flux expressions for each component in the respective cases are

$$J_1 = -D_{11}\frac{n_1}{\hat{f}_1}\frac{\mathrm{d}\hat{f}_1}{\mathrm{d}z}$$

$$\alpha = -D_{11}n_m\frac{\mathrm{d}\ln(1 + K_1(1 + \alpha_1\hat{f}_2)\hat{f}_1 + K_2\hat{f}_2)}{\mathrm{d}z} \quad (\text{fixed } \hat{f}_2) \tag{21a}$$

and

$$J_2 = -D_{22}\frac{n_2}{\hat{f}_2}\frac{\mathrm{d}\hat{f}_2}{\mathrm{d}z}$$

$$= -D_{22}n_m\frac{\mathrm{d}\ln(1+K_1\hat{f}_1+(K_2 + K_1\alpha_1\hat{f}_1)\hat{f}_2)}{\mathrm{d}z} \quad (\text{fixed } \hat{f}_1) \tag{21b}$$

which may be integrated to obtain the permeabilities:

$$P_1 = \frac{D_{11}n_m}{\hat{f}_1(\mathrm{I}) - \hat{f}_1(\mathrm{II})}\ln\left[\frac{1 + K_1(1 + \alpha_1\hat{f}_2)\hat{f}_1(\mathrm{I}) + K_2\hat{f}_2}{1 + K_1(1 + \alpha_1\hat{f}_2)\hat{f}_1(\mathrm{II}) + K_2\hat{f}_2}\right], \tag{22a}$$

and

$$P_2 = \frac{D_{22}n_m}{\hat{f}_2(\mathrm{I}) - \hat{f}_2(\mathrm{II})}\ln\left[\frac{1 + K_1\hat{f}_1 + (K_2 + K_1\alpha_1\hat{f}_1)\hat{f}_2(\mathrm{I})}{1 + K_1\hat{f}_1 + (K_2 + K_1\alpha_1\hat{f}_1)\hat{f}_2(\mathrm{II})}\right], \tag{22b}$$

where $\hat{f}_i(\mathrm{I})$ and $\hat{f}_i(\mathrm{II})$ are the fugacities of component i within the control volumes on either side of the infinitely thick membrane. The results shown as the horizontal dashed lines tagged with the filled and open squares in Fig. 6(a) correspond to Eqs. (22a) and (22b) respectively with $D_{11}=0.266\times10^{-8}$ m^2/s and $D_{22}=0.682\times10^{-8}$ m^2/s.

For the isobaric counterdiffusion case the infinite system permeabilities are estimated as follows. Within the control volumes on both sides of the membrane the equilibrium bulk Gibbs–Duhem equation provides

$$\mathrm{d}\hat{f}_{1B} + \frac{\hat{\phi}_{1B}}{\hat{\phi}_{2B}}\mathrm{d}\hat{f}_{2B} = 0, \tag{23}$$

where $\hat{\phi}_{iB}$ is the fugacity coefficient of component i in the bulk gas mixture. From a limited amount of data on the bulk properties of the simulated hydrogen–methane gas mixtures it was found that the fugacity coefficient ratio $\hat{\phi}_{1B}/\hat{\phi}_{2B}$ is essentially independent of composition and is within a few per cent of 1.0 at the temperature and pressure of the counterdiffusion simulations. Based on these observations we have to a good approximation $\hat{f}_{1B} + \hat{f}_{2B} \approx$ constant(= 0.037, on average, in units of kT/Δ^3) and therefore $\Delta\hat{f}_{1B} = -\Delta\hat{f}_{2B}$. Under these conditions the flux ratio is (see Eq. (11)):

$$J_1/J_2 = -P_1/P_2 \quad (\text{fixed pressure}). \tag{24}$$

Combining this result with Eq. (19c) for both species provides the following relationships for the intrapore fugacities:

$$\frac{\mathrm{d}\hat{f}_1}{\mathrm{d}\hat{f}_2} = -\frac{P_1}{P_2}\frac{(\hat{f}_1/n_1)}{(\hat{f}_2/n_2)}\left[\frac{D_{22} + (P_2/P_1)D_{12}}{D_{11} + (P_1/P_2)D_{21}}\right], \tag{25a}$$

and the fluxes

$$J_1 = -\left[\frac{D_{11}D_{22} - D_{12}D_{21}}{D_{22} + (P_2/P_1)D_{12}}\right]\frac{n_1}{\hat{f}_1}\frac{\mathrm{d}\hat{f}_1}{\mathrm{d}z} = -D_{1p}\frac{n_1}{\hat{f}_1}\frac{\mathrm{d}\hat{f}_1}{\mathrm{d}z}, \tag{25b}$$

$$J_2 = -\left[\frac{D_{11}D_{22} - D_{12}D_{21}}{D_{11} + (P_1/P_2)D_{21}}\right]\frac{n_2}{\hat{f}_2}\frac{\mathrm{d}\hat{f}_2}{\mathrm{d}z} = -D_{2p}\frac{n_2}{\hat{f}_2}\frac{\mathrm{d}\hat{f}_2}{\mathrm{d}z}. \tag{25c}$$

Using the adsorption isotherms and the correlated results for the diffusion coefficients then Eq. (25a) may be numerically integrated with the permeability ratio as a fitting parameter. For the case of the infinitely thick membrane it may be assumed that the pore mouth resistances to mass transfer are negligible and therefore to satisfy the boundary conditions within control volumes I and II it may be shown that the best fit estimate for the ratio P_1/P_2 is 49.6. The permeability of methane in a pore of infinite length is then obtained by integrating Eq. (25b), i.e.

$$P_1 = \frac{1}{(\hat{f}_1(\mathrm{I}) - \hat{f}_1(\mathrm{II}))}\int_{\hat{f}_1(\mathrm{II})}^{\hat{f}_1(\mathrm{I})} D_{1p}\frac{n_1}{\hat{f}_1}\mathrm{d}\hat{f}_1. \tag{26}$$

The result predicted by this expression (3.66×10^{-8} m^2/s) is shown as the dashed line tagged by full squares in Fig. 6(b). The hydrogen counterdiffusion permeability (P_2=7.37×

10^{-10} m^2/s) under similar conditions corresponds to the dashed line tagged by open squares. It is of interest to note that this result for P_2 is approximately a factor of five smaller than the value obtained for a similar hydrogen chemical potential difference under forced flow conditions and it is readily shown that the source of this hindrance effect is the cross-coupling term appearing in the denominator of the first expression on the right of Eq. (25c).

For very short pores the pressure driven transport results reported in Fig. 6(a) show that the hydrogen permeability is significantly larger than the methane permeability although this picture is reversed for pore lengths greater that 1 nm. As the pore length increases beyond this value the hydrogen permeability passes through a maximum and slowly approaches the result predicted for forced flow in infinitely long pores. In contrast, the methane permeability increases monotonically with pore length and it would appear that pore lengths (membrane thicknesses) of the order of tens or hundreds of nanometers are required to eliminate the influence of the pore entrance and exit on the permeation process. The results for the methane permeability are well correlated by the simple expression:

$$\frac{1}{P_1} = \frac{1}{P_0(2L)} + \frac{1}{P_{1p}}, \tag{27}$$

where P_0 is the pore mouth conductance (estimated to be 13.7 m/s) and P_{1p} is the intrapore permeability given by the infinite system result. Eq. (27) suggests that the influence of the pore mouth resistance to mass transfer is reduced to 1% of the overall resistance only for pores longer than 0.3 μm. One should bear in mind however that the pores under investigation in this work are highly idealised and it is quite possible that structural defects similar to those considered in [12] exist within the pores of real carbon membranes.

The fact that the coupling term in Eq. (19c) for the methane flux is negligible is emphasised by comparing the results for the methane permeability obtained both from the forced flow simulations (Fig. 6(a)) and from the isobaric counterdiffusion studies (Fig. 6(b)). The dashed line through both sets of results is essentially the same except for minor differences associated with the term P_{1p} in Eq. (27). However, while the presence of hydrogen has no effect on the methane flux it is clear, as noted above, that the sorbed methane has a very significant effect on the counterdiffusing hydrogen.

Another approach which may be employed to extract information from the NEMD simulations is to consider the concentration profiles within the permeable region between the two control volumes and a number of examples of these profiles are provided in Fig. 7. Methane concentration profiles under forced flow conditions are shown for three different pore lengths in Fig. 7(a) and these results suggest that reliable effective intrapore diffusivities may be obtained for pores of length $2L$=1.562 nm or greater by fitting the central portion of the profiles in the vicinity of z=0 to the

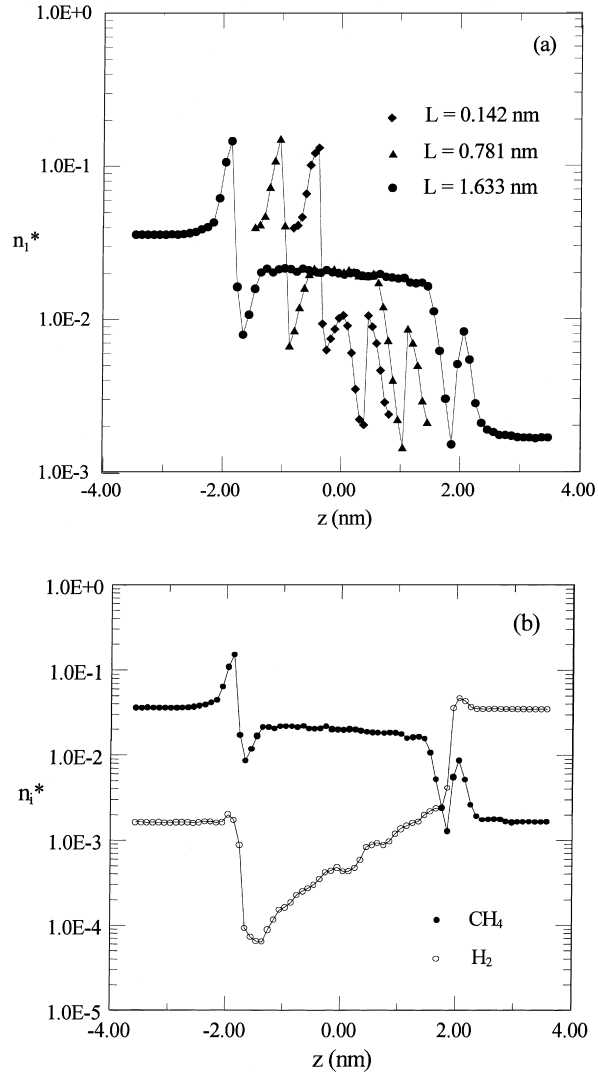

Fig. 7. Concentration profiles through the pores. (a) Methane density profiles for three pore lengths under forced flow conditions (fixed H_2 fugacity); (b) methane and hydrogen profiles within the pore of length $2L$=3.266 nm under isobaric conditions.

expression:

$$J_1 = -D_{1,\mathrm{eff}}\frac{n_1}{kT}\frac{\mathrm{d}\mu_1}{\mathrm{d}z} - D_{1,\mathrm{eff}}\frac{n_1}{\hat{f}_1}\frac{\mathrm{d}\hat{f}_1}{\mathrm{d}z}$$
$$= D_{1,\mathrm{eff}}n_m\frac{\mathrm{d}\ln(1-(n_1/n_m))}{\mathrm{d}z}, \tag{28}$$

where it has been assumed that viscous shear effects are negligible. The results obtained for methane at fixed hydrogen fugacity and from a similar analysis of the hydrogen profiles at fixed methane fugacity are reported in Fig. 8(a). The tagged dashed lines in this figure again provide the results for the infinite system diffusivities D_{ii} at densities corresponding to the centreline values in the finite length pores and quite clearly the viscous terms do not contribute significantly to the fluxes.

The concentration profiles shown in Fig. 7(b) (as well as those for $2L$=1.562 nm and $2L$=2.414 nm) for isobaric

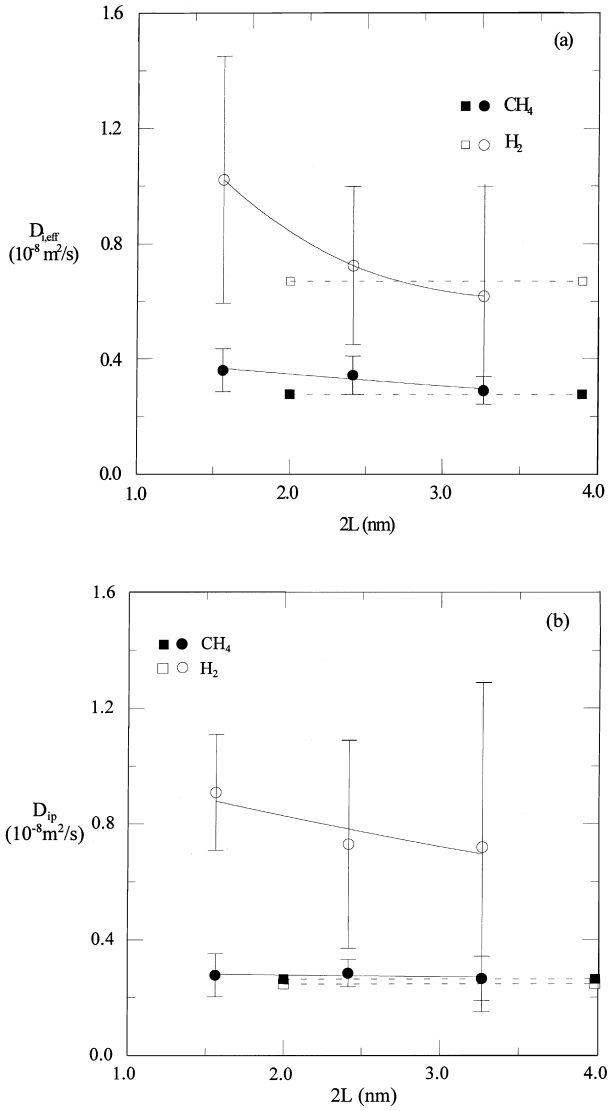

Fig. 8. Centreline diffusivities for the three longest pores as functions of pore length. (a) Effective diffusivities, $D_{i,\mathrm{eff}}$, for methane and hydrogen under forced flow conditions estimated using Eq. (28); (b) pore diffusivities as defined by Eqs. (25a), (25b) and (25c) under isobaric conditions.

diffusion conditions were similarly considered using Eqs. (25b) and (25c)). From the known concentrations and the adsorption isotherms it was possible to compute and fit the fugacity profiles for the species in the vicinity of $z=0$ and the results obtained from Eqs. (25b) and (25c)) for the pore diffusivities D_{ip} are shown in Fig. 8(b). The infinite system predictions for the same concentrations at the centreline of the finite length pore are $D_{11}=0.266\times10^{-8}$ m^2/s, $D_{22}=0.489\times10^{-8}$ m^2/s, $D_{12}=0.232\times10^{-8}$ m^2/s, and $D_{21}=0.53\times10^{-10}$ m^2/s and the predicted values for D_{ip} are shown as the dashed lines. The agreement between the methane results for the finite and infinite length pores is excellent and it should also be noted that the cross-diffusion terms in the expression for D_{1p} play a very minor role in its estimation. This is not the case, however, for the infinite system pore diffusivity for hydrogen which is predicted to be a factor of two lower than the uncoupled value, D_{22}. Furthermore, a serious ambiguity appears to arise in the case of D_{2p} for finite length pores and at this time we can only conclude that in contrast to the methane flux, the theoretical expression for the flux of hydrogen within these comparatively short pores cannot be simply represented by the result for the infinite system. This may be interpreted qualitatively in terms of an argument similar to that proposed in [33] in which it was concluded that a premature break in the intrapore momentum correlations of the diffusing particles as they leave pores of finite length results in a larger apparent diffusion coefficient. The latter effect should be particularly noticeable for small, weakly adsorbing particles (as observed for hydrogen) whereas particle/pore wall thermal diffuse scattering of a strongly adsorbing component encourages a rapid decay of the molecular correlation functions in a manner analogous to an infinite system even if the pore is comparatively short.

While the general features of the results obtained from the NEMD simulations are in good qualitative agreement with experimental observations for forced flow separation using carbon membranes [20,21], a direct quantitative comparison with experimental data cannot be made for a number of reasons (pressure gradients at least an order of magnitude lower are involved in the experiments and the pore structure within the real carbon membranes is presumably much more complex). Nevertheless the following estimates for a single pore of infinite length provide guidelines with respect to the efficacy of the modelling techniques employed in this work. At low pressures the relative permeabilities of the two pure gases, $P_1/P_2=(D_{11}K_1)/(D_{22}K_2)$, is 4.2 (273.15 K) in good agreement with the experimental value 5.1 (295.1 K). Under these conditions the hydrogen 'diffusivity' (which, based on the definitions employed in [20,21], is equivalent to our $D_{22}K_2n_m$) is predicted to be 4.2×10^{-8} m^2/s (273.15 K) while the experimental value is 2.96×10^{-10} m^2/s (295.1 K). We believe the experimental result is much lower due to porosity/tortuosity effects which have not been incorporated into the theoretical value in addition to the influence of structural heterogeneities within the real carbon such as carbon lattice dislocations, variable pore cross-sections (similar to the pore entrance and exit resistances involved with the short pores investigated in the NEMD simulations) etc. The NEMD simulations do, however, confirm that the selectivity mechanism is directly related to partial pore blockage by the more strongly adsorbing species. For the model pore considered here the hydrogen permeability in the mixed gas case (the (b) series of simulations) is reduced by at least an order of magnitude relative to the value for pure hydrogen.

4. Summary

Binary transport of hydrogen and methane mixtures within a comparatively simple model carbon membrane

has been simulated in this work. The results obtained demonstrate the principal underlying features of the separation mechanism and the utility of the nonequilibrium molecular dynamics method. Pore entrance/exit resistances to mass transfer would appear to be significant if the pores controlling the separation process within real carbon membranes are relatively short (less than 0.1 μm in length). Furthermore, for the very small pores present in these microporous carbons we believe the viscous shear contribution to the species fluxes is negligible in comparison with the diffusive terms. While the latter conclusion has been widely accepted in the literature primarily on the basis of the dependence of the parameter B_0 in the viscous term on the square of the pore width, the results obtained from the NEMD method employed in this work verify this assumption from a molecular perspective. The influence of cross-coupling on the transport of the strongly adsorbing, heavier methane particles was also generally found to be negligible whereas a significant reduction in the flux of hydrogen due to cross-coupling was observed during isobaric counter-diffusion. Finally, for finite pore lengths it was observed that while methane intrapore transport was consistent with the predictions of linear nonequilibrium theory, the hydrogen diffusion coefficients were systematically larger, particularly for very short pores.

5. Nomenclature

a	acceleration (m/s^2)
B_0	viscous flow coefficient (m^2)
D	phenomenological diffusion coefficient (m^2/s)
$Đ$	Stefan–Maxwell binary diffusion coefficient (m^2/s)
E	energy (J)
E_{ij}	interaction parameter which depends on the strength of the adsorption field
F^+	unidirectional particle flux normal too and away from the collisional tangent plane
$\hat{f}$	fugacity (in units of kT/Δ^3)
g	contact pair correlation function
J, **J**	flux (particles/m^2 s)
k	Boltzmann's constant
K	equilibrium adsorption coefficient (in units of Δ^3/kT).
L	pore half-length (nm)
L_{ij}	phenomenological coefficient (s/kg m^2)
m	particle mass (kg)
n	particle number density (particles/m^3)
n^*	reduced number density $n\Delta^3$
N	particle number
p	pressure N/m^2
P	permeability (m^2/s)
P_0	pore mouth conductance (m/s)
r_{ij}	relative separation of particles i and j (nm)
r_{cut}	cut-off radius for particle–particle interaction (nm)
r	particle coordinate (m)
R	particle radius (nm)
S	selectivity
t	time (s)
T	temperature (K)
v	particle velocity (m/s)
V	volume (m^3)
w	pore width (nm)
x,y,z	cartesian coordinates (m)
α	polar angle
Δ	interplane spacing in graphite (0.335 nm)
ε	potential minimum in the Lennard-Jones (12–6) potential function (J/particle)
η	shear viscosity (N s/m^2)
θ	polar angle
φ	polar angle
μ	chemical potential (J/particle)
ξ	uniformly distributed random number
σ	Lennard-Jones (12–6) diameter (nm)
ϕ	potential interaction energy (J)
ϕ	polar angle
Φ	system potential energy (J)

Subscripts

c	carbon
B	bulk fluid state
i	species or particle index
j	species or particle index
m	monolayer
1	methane
2	hydrogen

References

[1] E.A. Mason, L.A. Viehland, Statistical mechanical theory of membrane transport for multicomponent systems: passive transport through open membranes, J. Chem. Phys. 68 (1978) 3562–3573.
[2] E.A. Mason, A.P. Malinauskas, Gas Transport in Porous Media: The Dusty Gas Model, Elsevier, Amsterdam, 1983.
[3] R. Krishna, J.A. Wesselingh, The Maxwell–Stefan approach to mass transfer, Chem. Eng. Sci. 52 (1997) 861.
[4] J. Karger, D.M. Ruthven, Diffusion in Zeolites and Other Microporous Solids, Wiley, New York, 1992.
[5] E.J. Maginn, R.Q. Snurr, A.T. Bell, D.N. Theodorou, Simulation of hydrocarbon diffusion in zeolites, in: H. Chon, S.-K. Ihm, Y.S. Uh (Eds.), Progress in Zeolite and Microporous Materials, vol. 105, Elsevier, Amsterdam, 1997, p. 1851.
[6] J.M.D. MacElroy, K. Raghavan, Adsorption and diffusion of a Lennard-Jones vapor in microporous silica, J. Chem. Phys. 93 (1990) 2068.
[7] J.M.D. MacElroy, K. Raghavan, Transport of an adsorbing vapour in a model silica system, J. Chem. Soc., Faraday Trans. 87 (1991) 1971.
[8] A. Brodka, T.W. Zerda, Molecular dynamics of SF_6 in porous silica, J. Chem. Phys. 95 (1991) 3710.
[9] J.M.D. MacElroy, N.A. Seaton, S.P. Friedman, Sorption rate processes in carbon molecular sieves, Chapter 17, in: W. Rudzinski, W.A. Steele, G. Zgrablich (Eds.), Equilibria and Dynamics of Gas Adsorption on Heterogeneous Solid Surfaces, Elsevier, Amsterdam, 1997.

[10] N.A. Seaton, S.P. Friedman, J.M.D. MacElroy, B.J. Murphy, The molecular sieving mechanism in carbon molecular sieves, Langmuir 13 (1997) 1199–1204.
[11] J.M.D. MacElroy, N.A. Seaton, S.P. Friedman, On the origin of transport resistances within carbon molecular sieves, Chem. Eng. Sci. 54 (1999) 1015–1027.
[12] P. Neogi, Diffusion in Polymers, Marcel Dekker, New York, 1996.
[13] D.A. Mooney, J.M.D. MacElroy, Theoretical studies of the structure and dynamics of semi-crystalline PPTA/water vapour interfaces, Langmuir 13 (1997) 1173–1181.
[14] M.P. Allen, D.J. Tildesley, Computer Simulation of Liquids, Clarendon Press, Oxford, 1987.
[15] J.M.D. MacElroy, Nonequilibrium molecular dynamics simulation of diffusion and flow in thin microporous membranes, J. Chem. Phys. 101 (1994) 5274.
[16] G.S. Heffelfinger, F. van Swol, Diffusion in Lennard-Jones fluids using dual control volume grand canonical molecular dynamics simulation (DCV-GCMD), J. Chem. Phys. 100 (1994) 7548.
[17] R.F. Cracknell, D. Nicholson, N. Quirke, Direct molecular dynamics simulation of flow down a chemical potential gradient in a slit-shaped micropore, Phys. Rev. Lett. 74 (1995) 2463.
[18] S. Furukawa, T. Shigeta, T. Nitta, Nonequilibrium molecular dynamics for simulating permeation of gas mixtures through nanoporous carbon membranes, J. Chem. Eng. Jpn 29 (1996) 725.
[19] D.M. Ford, E.D. Glandt, A molecular simulation study of the surface barrier effect: dilute gas limit, J. Phys. Chem. 99 (1995) 11543.
[20] M.B. Rao, S. Sircar, Nanoporous carbon membrane for gas separation, Gas Sep. Purif. 7 (1993) 279–284.
[21] M.B. Rao, S. Sircar, Nanoporous carbon membranes for separation of gas mixtures by selective surface flow, J. Membr. Sci. 85 (1993) 253.
[22] W.A. Steele, The Interaction of Gases with Solid Surfaces, Pergamon Press, Oxford, 1974.
[23] J.O. Hirschfelder, C.F. Curtiss, R.B. Bird, Molecular Theory of Gases and Liquids, Wiley, New York, 1954.
[24] D.J. Adams, Chemical potential of hard sphere fluids by Monte Carlo methods, Mol. Phys. 28 (1974) 1241–1252.
[25] D.J. Adams, Grand canonical ensemble Monte Carlo for a Lennard-Jones fluid, Mol. Phys. 29 (1975) 307–311.
[26] L. Verlet, Computer 'experiments' on classical fluids. I. Thermodynamical properties of Lennard-Jones molecules, Phys. Rev. 159 (1967) 98–103.
[27] S.-H. Suh, J.M.D. MacElroy, Molecular dynamics simulation of hindered diffusion in microcapillaries, Mol. Phys. 58 (1986) 445.
[28] J.M.D. MacElroy, S.-H. Suh, Computer simulation of moderately dense hard-sphere fluids and mixtures in microcapillaries, Mol. Phys. 60 (1987) 475.
[29] D.M. Ruthven, K.F. Loughlin, K.A. Holborow, Multicomponent sorption equilibrium in molecular sieve zeolites, Chem. Eng. Sci. 28 (1973) 701.
[30] C.S. Lee, J.P. O'Connell, Statistical mechanics of partially-mobile adsorption of gases on homogeneous solid surfaces, J. Colloid Interface Sci. 41 (1972) 415–429.
[31] J.L. Lebowitz, E. Helfand, E. Praestgaard, Scaled particle theory of fluid mixtures, J. Chem. Phys. 43 (1965) 774.
[32] S. Chapman, T.G. Cowling, The Mathematical Theory of Non-uniform Gases, 3rd ed., Cambridge University Press, Cambridge, 1970.
[33] J.M.D. MacElroy, S.-H. Suh, Self-diffusion in single-file pores of finite length, J. Chem. Phys. 106 (1997) 8595.